Nanoscale Advances

ROYAL SOCIETY OF CHEMISTRY

PAPER

View Article Online
View Journal | View Issue

Cite this: *Nanoscale Adv.*, 2021, **3**, 4858

Control of the interface graphitized/amorphous carbon of biomass-derived carbon microspheres for symmetric supercapacitors†

Hongqiang Wang, Xin Li, Jiming Peng, Yezheng Cai,* Juantao Jiang* and Qingyu Li

Rational interface control of porous carbon electrode materials is of significance for achieving efficient supercapacitors. Herein, biomass-derived carbon microspheres with a highly graphitized porous surface and amorphous subsurface were well constructed *via* a flexible coupled catalysis-activation process. The unique structure not only endows the carbon microspheres with rapid electron transfer but also an ultra-high specific surface area. Owing to the optimized graphitized/amorphous structure, the obtained graphitized and activated starch-derived carbon microspheres display obviously impressive energy storage capability among the reported starch-derived carbon materials, even though they were evaluated in a narrow voltage window. The assembled symmetrical supercapacitor based on the optimized carbon microspheres exhibits a high capacitance of 198 F g^{-1} at 1 A g^{-1}, a high energy density of 14.67 W h kg^{-1} at a power density of 4142.80 W kg^{-1}, robust cycle performance, and good rate performance in alkaline aqueous electrolyte. This work provides a strategy for flexible construction of biomass-derived carbon electrode materials, with an optimized graphitized/amorphous and porous structure, for boosted energy storage in supercapacitor applications.

Received 9th April 2021
Accepted 29th June 2021

DOI: 10.1039/d1na00262g

rsc.li/nanoscale-advances

1. Introduction

Developing efficient energy storage technology is central to overcoming the intermittent and regional issues of renewable energy such as solar and wind energy. Supercapacitors, which store energy through adsorption/desorption of electrolyte ions and/or faradaic redox reactions, possess unique merits of high power density and fast charge/discharge capability, showing promising potential as energy storage devices for portable and stationary electronics.[1–3] However, the relatively low energy density and/or unsatisfactory electrochemical stability pose large challenges in this field.[4]

The adopted electrode material directly determines the energy storage capacity of supercapacitors. Given the unique features of good electronic conductivity, low cost, rich pore structures, and good chemical stability, porous carbon-based materials are a class of promising electrode materials for supercapacitors.[5–10] Regrettably, carbon-based supercapacitors generally exhibit low energy density (usually below 10 W h kg^{-1}) mainly due to the internal energy storage mechanism in which energy storage occurs only at the carbon electrode surface.[11] To overcome this obstacle, increasing the specific capacitance of porous carbon is highly needed according to the energy density equation.[12] Exposing more electrochemical active sites by constructing porous carbon with a large specific surface area (SSA) represents a feasible and universal strategy to boost the electrical storage capacity.[13] However, achieving a balance between the SSA and electronic conductivity and/or structural stability remains challenging. On the one hand, porous carbon with a large SSA usually contains a considerable part of amorphous carbon, which is not conducive to fast electron transfer and structure maintenance during frequent charging and discharging. On the other hand, porous carbon having an excessive degree of graphitization generally exhibits decreased density of active sites and therefore decreased specific capacitance. A combination of a high graphitization degree and suitable amorphous structure in porous carbon may achieve the target of enhanced energy storage capability.[14]

Biomass-derived porous carbon microspheres have attracted great interest for use as electrode materials due to their rich sources and excellent electrochemical performance in supercapacitors.[1,13,15,16] Flexible construction of biomass-derived carbon microspheres simultaneously possessing a large enough SSA and high graphitization degree is highly desirable, but it is still challenging.[17] Herein, by using renewable biomass potato starch as a carbon source, a coupled catalysis-activation process was proposed to construct carbon microspheres with a highly graphitized porous surface and amorphous subsurface. This

Guangxi Key Laboratory of Low Carbon Energy Materials, School of Chemistry and Pharmaceutical Sciences, Guangxi Normal University, Guilin, 541004, China. E-mail: yezhengcai@163.com; jtjiang@.gxnu.edu.cn

† Electronic supplementary information (ESI) available. See DOI: 10.1039/d1na00262g

unique structure endows the carbon microspheres with rapid ion/electron transfer and an ultra-high specific surface area, which can cooperatively improve the energy storage capacity of supercapacitors with increased specific capacitance, higher energy density, and good rate capacity. This work provides an effective strategy for optimizing the rapid ion/electron transfer microenvironment of carbon microsphere electrode materials for boosting energy storage performance.

2. Experimental

2.1 Materials

Potato starch was purchased from Shanghai Yuanye Biological Technology Co., Ltd. Ammonium phosphate $(NH_4)_2HPO_3$, potassium hydroxide (KOH), ferrous chloride tetrahydrate ($FeCl_2 \cdot 4H_2O$), cobaltous chloride hexahydrate ($CoCl_2 \cdot 6H_2O$), nickel(II) chloride hexahydrate ($NiCl_2 \cdot 6H_2O$), polytetrafluoroethylene alcohol solution (PTFE, 60 wt%), ethanol, acetylene black, and hydrochloric acid (HCl) were purchased from Aladdin.

2.2 Preparation of potato starch-based carbon microspheres

10.00 g Potato starch was immersed in 50 mL 20 wt% $(NH_4)_2HPO_3$ solution for 1 h, filtered, and freeze-dried to remove residual moisture. Then the cleaned starch PS sample was heated to 250 °C at a heating rate of 0.2 °C min^{-1} followed by heating to 450 °C (1 °C min^{-1}) and held at this temperature for 4 h under Ar in a tube furnace. The obtained black solid product was sieved (150 mesh) to obtain potato starch-derived carbon microspheres and was denoted as SC.

2.3 Preparation of graphitized and activated SC (GASC)

1.00 g SC was mixed well with suitable KOH (2.00 g) and $FeCl_2 \cdot 4H_2O$ (0.20 g) in deionized water, sonicated for 30 min, and dried at 80 °C. The mixture was then heated to 800 °C (3 °C min^{-1}) and held at this temperature for 1.5 h in Ar and naturally cooled down to room temperature. Next, the heated sample was washed with diluted HCl and deionized water to remove residual inorganic impurities, and dried at 80 °C to obtain Fe-catalyzed GASC which was denoted as GASC-Fe.

GASC-Co and GASC-Ni were synthesized in a similar manner to GASC-Fe by replacing $FeCl_2 \cdot 4H_2O$ with cobaltous chloride hexahydrate $CoCl_2 \cdot 6H_2O$ and $NiCl_2 \cdot 6H_2O$. GASC5, GASC10, and GASC15 with different $FeCl_2 \cdot 4H_2O$/SC mass ratios of 0.05/1.00, 0.10/1.00, and 0.15/1.00 were synthesized in a similar manner to GASC-Fe. For convenient comparison, GASC-Fe was also denoted as GASC20. PS-derived active carbon (AC) microspheres were also synthesized in a similar manner to GASC without the addition of metal precursors for comparison.

2.4 Characterization

The morphological features of the samples were characterized using a field-emission scanning electron microscope (SEM, FEI Quanta 200 FEG) and transmission electron microscope (TEM, JEOL 2011). Elemental distribution mapping was performed by energy dispersive spectroscopy (EDS) coupled with SEM. The crystal structure was determined by X-ray diffraction (XRD, Rigaku D/max 2500) with Cu Kα radiation ($k = 1.5406$ Å) operating at 40 kV. Raman measurements were performed by laser Raman spectroscopy (Jobin Yvon, T6400). X-ray photoelectron spectroscopy (XPS) was carried out using an AXIS ULTRA DLD instrument with aluminum Kα X-ray radiation. The resistance test was carried out on a semiconductor powder resistance tester ST2722 (JINGGE Electronics Co., Ltd, Suzhou, China). The Brunauer–Emmett–Teller (BET) specific surface area and pore features were determined using nitrogen adsorption desorption (JW-BK 122W, JWGB, China) at 77 K.

2.5 Electrochemical tests

GASC, PTFE (60 wt%), and AB with a mass ratio of 8 : 1 : 1 were well dispersed in ethanol and dried at 80 °C. The sludge mixture was pressed into a sheet and subsequently cut into 12 mm electrode pieces using a puncher and dried at 80 °C for 1 h. The mass loading of the electrodes is 2.21 mg cm^{-2}. A symmetric supercapacitor (SS) was assembled by assembling two identical electrodes using KOH (6 M) as the electrolyte.[4] The electrochemical performance of supercapacitor battery SS was examined by a galvanostatic charge–discharge test (GCD) at 0–0.8 V, a cyclic voltammetry test (CV) with different scan rates (10–100 mV s^{-1}), and impedance measurements (EIS) from 0.01 Hz to 100 kHz with an amplitude of 5 mV on an electrochemical workstation (IM6). The cyclic performance test was conducted on a Land battery measurement system (LAND BT2013A). The specific capacity of the SS was calculated according to eqn (1).[16]

$$C = (I \times \Delta t)/(\Delta V \times m) \quad (1)$$

where I (A) is the current density, m (g) is the total mass of two electrodes, Δt (s) is the discharge time (s), and ΔV (V) is the discharge potential.[4,18,19]

The energy density (E, W h kg^{-1}) and power density (P, W kg^{-1}) of the assembled SS were calculated according to eqn (2) and (3).

$$E = C \times \Delta V^2/(2 \times 3.6) \quad (2)$$

$$P = 3600E/\Delta t \quad (3)$$

3. Results and discussion

GASC electrode materials were synthesized by combing pre-carbonization and *in situ* catalytic graphitization–activation processes. Briefly, SC was obtained by pyrolysis of a mixture of PS and $(NH_4)_2HPO_3$ and then heated at high temperature with the introduction of a suitable Fe/Co/Ni precursor and KOH. A dilute acid treatment was further carried out to remove the introduced metal particles (Fig. 1a). Pre-carbonization experiments indicate that low temperature pyrolysis with a slow heating rate was necessary to obtain carbon microspheres, and a fast heating rate led to the formation of large irregular carbon blocks which is not conductive to the exposure of the specific

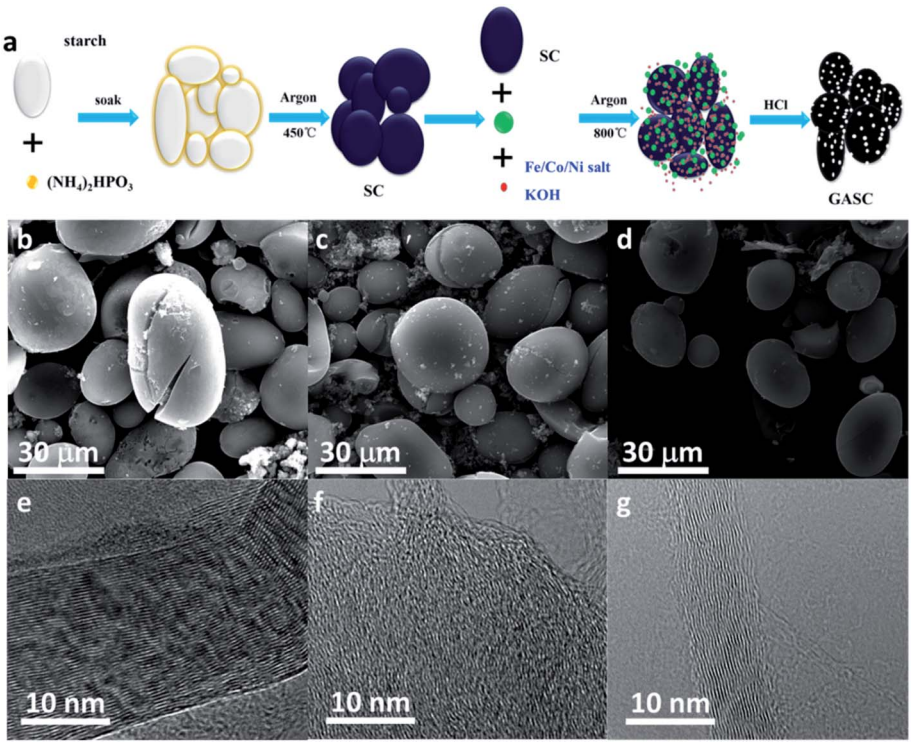

Fig. 1 (a) Schematic of the synthesis of GASC; (b–g) SEM and HRTEM images of GASC-Fe (b and e), GASC-Co (c and f), and GASC-Ni (d and g).

surface area for energy storage (seen in Fig. S1†). The SEM images (Fig. S2a–c† and 1b–d) of the GASC-Fe, GASC-Co, and GASC-Ni samples show that carbon microspheres with crackles can be maintained after further catalytic graphitization similar to SC. Notably, additional loose and porous carbon fragments located on the surface of carbon microspheres and cracked carbon microspheres can be observed, which are beneficial for the exposure of the specific surface area and electron transfer for enhancing energy storage. TEM images (Fig. S2d–f†) demonstrate the formation of carbon sheets without metal particles in these samples, suggesting successful removal of Fe/Co/Ni species after acid treatment. High resolution TEM images (Fig. 1e–h) reveal that additional lattice fringes corresponding to the C (002) plane can be clearly distinguished at the surface of these samples, suggesting a high graphitization degree. Furthermore, GASC-Fe displays thicker surface longitudinal graphitized carbon than GASC-Co and GASC-Ni, signifying more effective catalytic graphitization.

To reveal the influence of the Fe salt content on the catalytic graphitization effect of the final GASC, GASC5, GASC10, and GASC15 with different mass ratios of Fe salt/SC were synthesized in a similar manner to GASC-Fe, and PS-derived active carbon (AC) microspheres were also synthesized in a similar manner to GASC-Fe without the addition of the Fe precursor. The SEM images (Fig. 2a–d and S3†) indicate that these four samples all display a carbon microsphere shape similar to SC. Note that excess iron salt will destroy the original microspheres and therefore lead to the formation of irregular shape carbon blocks (see the SEM image of GASC15 in Fig. S3c†), suggesting the significance of the Fe salt ratio in tuning the microscopic features. The partial structural collapse of carbon microspheres in GASC15 is mainly due to excessive catalytic graphitization from excess Fe catalyst. As seen in TEM images (Fig. 2e–h), thin carbon sheets with some metal particles were formed in GASC5, GASC10, and GASC15 but not in AC. The HRTEM image (Fig. 2i) indicates that no carbon lattice fringes can be found in AC. In contrast, clear carbon lattice fringes observed in HRTEM images (Fig. 2j–l) of GASC5, GASC10, and GASC15 confirm the enhanced graphitization of the carbon matrix.

To understand the crystal structure characteristics, the synthesized GASC and AC samples were examined by XRD. As displayed in Fig. S4a,† the XRD patterns of AC display two gentle peaks at ~26° and 44° corresponding to the (002) and (100) planes of the carbon material, indicating amorphous structures; however, the intensity of these two peaks obviously increased when Fe salt was introduced as seen from the XRD patterns of GASC-Fe, GASC-Co, and GASC-Ni, suggesting an enhanced graphitization degree due to the catalytic graphitization process of carbon species during heat treatment. Note that the (002) peak of GASC-Fe is sharper than that of GASC-Co and GASC-Ni, implying that Fe is more effective for catalytic graphitization of PS-derived carbon which is consistent with the result of HRTEM (Fig. 1e–g). The XRD patterns (Fig. 3a) of GASC05, GASC10, GASC15, and GASC20 further indicate that these peaks became sharper with the increase of the Fe salt ratio along with lattice contraction (Table S1†), confirming the robust effect of catalytic graphitization by metallic Fe, which was *in situ* formed from the Fe salt reduced by PS-derived reducing substances. Besides, no additional diffraction peaks can be seen from the XRD patterns of the GASC samples when compared to

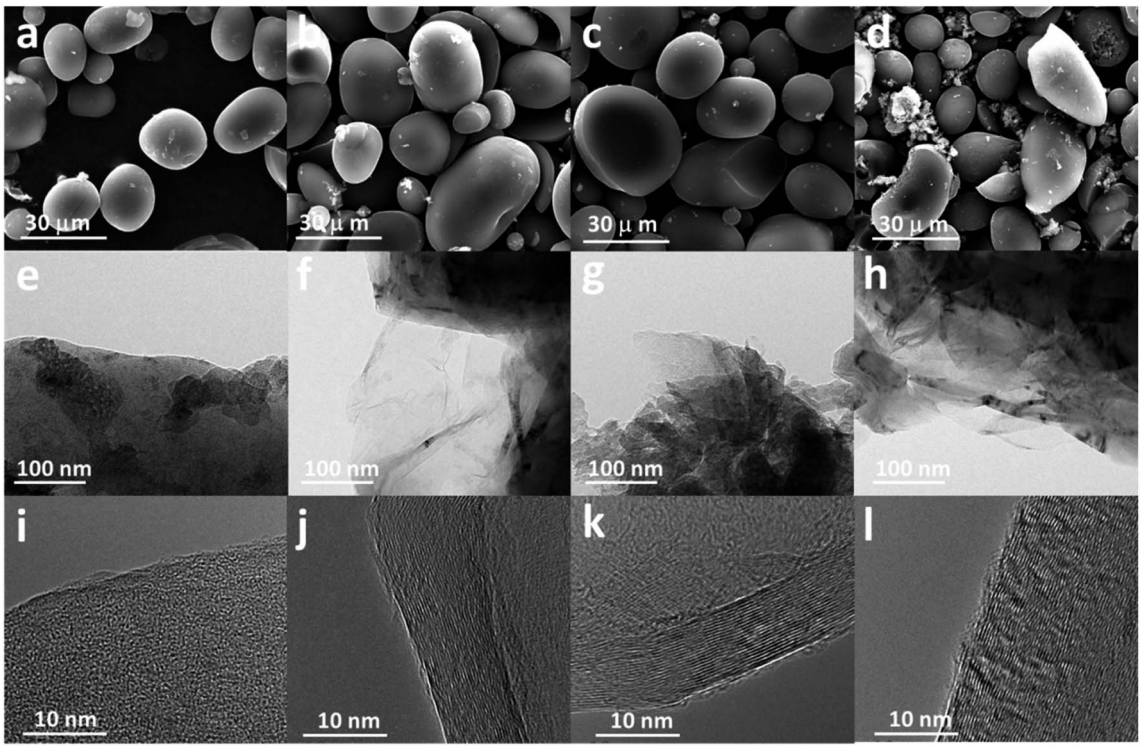

Fig. 2 SEM, TEM, and HRTEM images of AC (a, e and i), GASC5 (b, f and j), GASC10 (c, g and k), and GASC15 (d, h and l).

AC, demonstrating the absence of metal and/or metal oxides. The enhanced graphitization degrees of the GASC samples were further confirmed from Raman spectra (Fig. S4b† and 3b), as evidenced from the decreased I_D/I_G value (Table S1†), which is the intensity ratio of the D band to the G band, of the GASC samples compared to AC, which is consistent with the XRD result.[20,21] Note that the appropriately enhanced graphitization degree benefits the electronic transfer and therefore promotes the electrochemical performance.

The pore structure features of the GASC and AC (Fig. S4c, d† and 3c) samples were characterized by N_2 adsorption–desorption isotherms. AC displayed a type-I isotherm curve indicating a microporous structure. However, all GASC samples exhibited combined characteristics of typical type I and IV isotherms with sharp and gentle adsorption behaviors at low and moderate pressures, indicating the existence of micropores and mesopores.[22,23] Note that micropores can promote the exposure of electrochemically active sites and the mesopores can boost the ion transfer. The GASC samples are highly expected to possess enhanced energy storage capability. The specific surface areas of AC and GASC samples calculated by the BET method are sufficiently large for achieving energy storage and the detailed pore features are provided in Table S1.† The tested samples have a vast majority of micropores with some mesopores. Notably, GASC10 (2369 $m^2 g^{-1}$) has the largest BET specific surface area among the tested samples, suggesting that appropriate control of the iron salt ratio benefits the maximum exposure of the specific surface area for promoting the electrochemical performance. A balance between the high graphitization and rich pore structure can be achieved by suitable surface catalytic graphitization.

The surface chemical features of the AC and GASC samples were explored by XPS. Fig. 3d shows the representative XPS survey spectra of AC and GASC10. These two samples only possess C and O elements with C/O atomic ratio of 77.63/22.37 for AC and 82.31/17.69 for GASC10. No other element or Fe species existed on the surface of GASC10, as further confirmed from the EDS spectra in the selected area of AC (Fig. S5†) and GASC10 (Fig. S6†). EDS mappings further reveal the distributions of C and O through the carbon microspheres. The high-resolution C 1s spectra (Fig. 3e–i) of the AC, GASC05, GASC10, GASC15, and GASC20 samples can be fitted into 4 peaks corresponding to C sp^2 (284.4 eV), C sp^3 (285.6 eV), C–O (286.2 eV) and COO– (288.6 eV), respectively.[1,24] The C sp^2 peak represents the orderly arranged carbon structure while the C sp^3 peak indicates the existence of disorderly arranged carbon. The increase in the C sp^2/sp^3 area ratio of GASC5, GASC10, GASC15, and GASC20 compared to that of AC indicates the enhanced graphitization degree trend, which is consistent with the above XRD and Raman results. Note that GASC10 exhibits a sharp increase in the C sp^2/sp^3 area ratio compared to AC and further increasing the Fe salt ratio during the high temperature activation process will not obviously increase the C sp^2/sp^3 area ratio. Hence, GASC10 has been highly graphitized.

Encouraged by the porous structure with abundant micropores and mesopores, the large specific surface area, and the high graphitization degree, the as-synthesized AC and GASC samples were highly expected to possess desirable energy storage capability. The electrochemical performance of

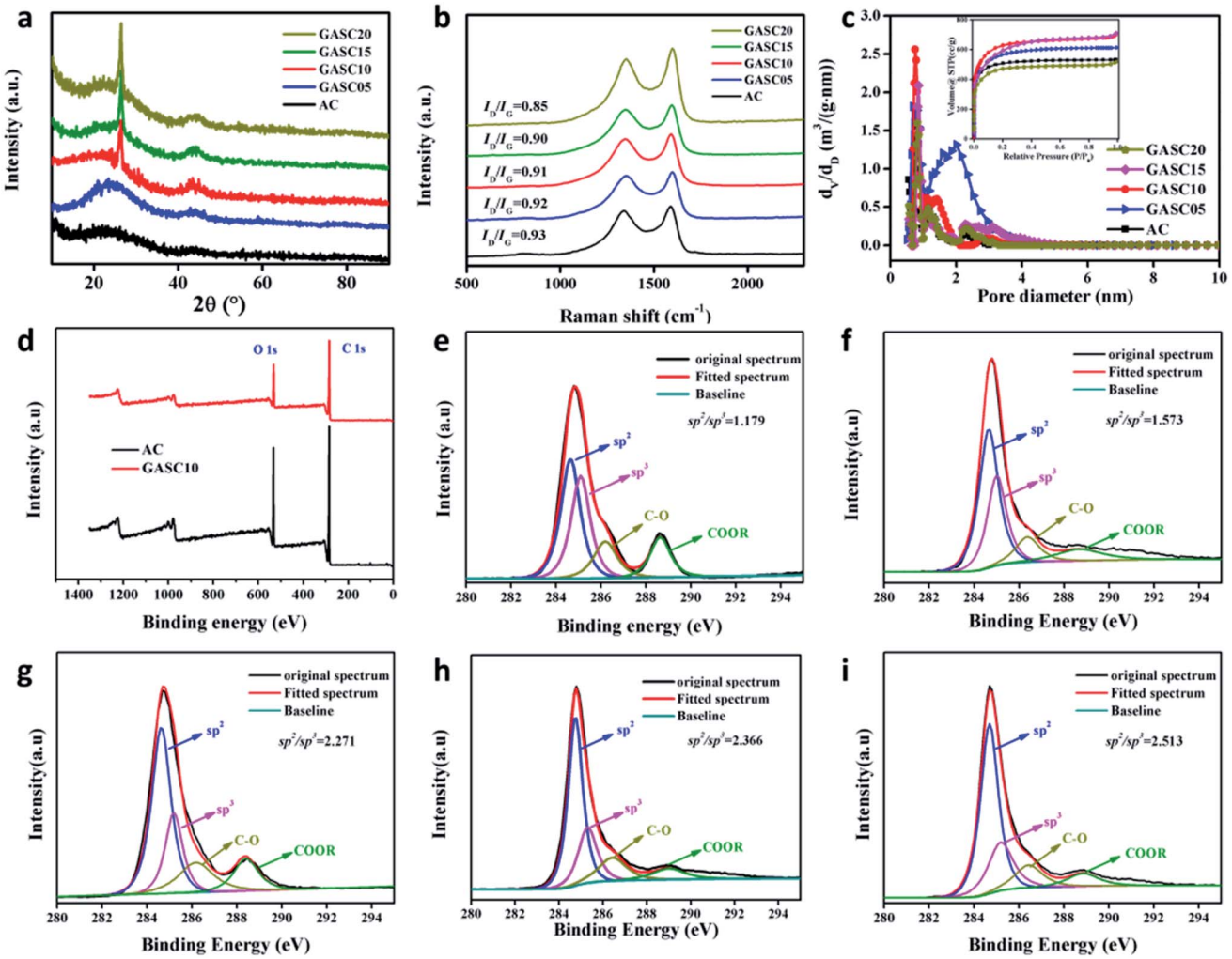

Fig. 3 (a) XRD patterns, (b) Raman spectra, (c) pore size distributions and N_2 adsorption–desorption isotherms (inset) of GASC samples; (d) XPS survey spectra of AC and GASC10; (e–i) high resolution C 1s spectra of AC (e), GASC05 (f), GASC10 (g), GASC15 (h), and GASC20 (i).

symmetrical supercapacitors (SSCs) using GASC-Fe, GASC-Co, and GASC-Ni samples as electrode materials was first evaluated by CV measurements and compared to that of an AC SSC as shown in Fig. 4a–d. All the CV curves of the AC, GASC-Fe, GASC-Co, and GASC-Ni SSCs exhibit a good quasi-rectangular shape even when the scan rate was increased from 10 mV to 100 mV, indicating the characteristics of good electric double layer capacitance and rapid ion transfer.[25] The GCD curves (Fig. 4e–h) displaying symmetrical isosceles triangle features demonstrate good electrochemical reversibility and high Coulomb efficiency. Regrettably, the discharging times of the GASC-Fe, GASC-Co, and GASC-Ni SSCs wereshorter than that of the AC SSC, implying relatively low specific capacitance mainly due to the difference in structural features. Notably, the GASC-Co SSC having a larger specific surface area and lower resistivity than the AC SSC exhibited smaller specific capacitance than AC (Fig. S7†), which can be mainly due to the relatively low graphitization degree (see Table S1†) and the smaller average pore width of GASC-Co (0.752 nm) calculated by the DFT method when compared to GASC-Fe (0.818 nm) and GASC-Ni (0.818 nm). The purpose of catalytic graphitization is to enhance electron transfer and structural stability for benefiting energy storage. However, excessive catalytic graphitization due to the addition of a high metal salt ratio during the high temperature activation process will destroy the mesopores which is unfavorable for ion transfer. This observation also indicates that the optimal pore structure with appropriate amounts of micropores and mesopores is critical in determining the energy storage capability of carbon materials. Therefore, a balance between the specific surface area and graphitization degree should be achieved by controlling the content of interface graphitized/amorphous carbon.

To optimize catalytic graphitization and the pore structure, Fe-catalyzed GASC05, GASC10, and GASC15 samples with different Fe salt ratios were synthesized in a similar manner to GASC-Fe. The CV curves of the AC, GASC05, GASC10, GASC15, and GASC20 samples in Fig. 5a indicate that GASC10 has the largest area among the tested samples, suggesting superior capacitance mainly due to the largest BET specific surface area (Table S1†). The CV curves of GASC10 at different scan rates

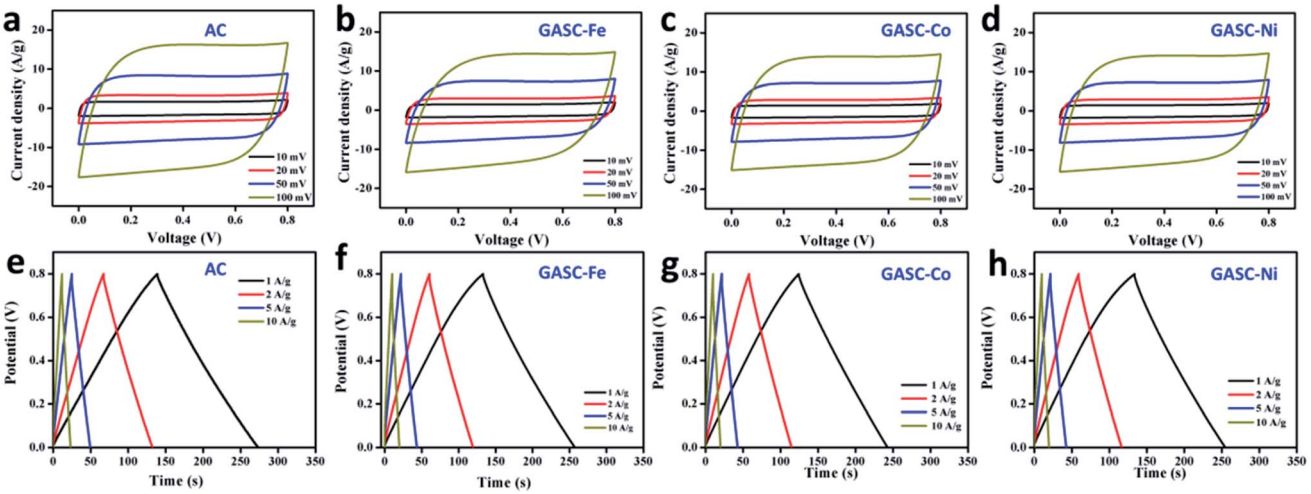

Fig. 4 CV curves at different scan rates and charge–discharge curves at different current densities of AC (a and e), GASC-Fe (b and f), GASC-Co (c and g), and GASC-Ni (d and h).

indicate good electrical double-layer capacitive (EDLC) behavior, as evidenced from the maintenance of a rectangular-like shape even when the scan rate was increased from 10 mV to 100 mV (Fig. 5b).[26] The GCD curves (Fig. 5c) of these five samples at a current density of 1 A g^{-1} showing symmetrical isosceles triangles suggest rapid electron transfer and desirable reversibility.[27] Remarkably, the GASC10 SSC exhibited the longest discharging time, confirming enhanced energy storage capability compared to the GASC20 SSC (here GASC20 is equal to GASC-Fe). The GCD curves (Fig. S8a–c†) of the AC, GASC05 and GASC10 SSCs at different current densities display a nearly symmetrical triangle shape indicative of EDLC behavior without pseudocapacitance, low internal resistance, and high Coulomb efficiency. However, the GCD curves (Fig. S8d and e†) of the GASC15 and GASC20 SSCs exhibited a slight ohmic drop mainly due to the decrease in specific surface area and mesopore ratio derived from excessive graphitization. The corresponding specific capacitance results calculated from the GCD curves displayed in Fig. 5d indicate that GASC10 exhibited higher specific capacitance than the other samples at different current densities, confirming superior energy storage capability. The enhanced energy storage capability of GASC10 can be attributed to the large specific surface area of GASC10 (2369 m^2 g^{-1}) compared to the other samples, such as GASC5 (1954 m^2 g^{-1}), GASC15 (2119 m^2 g^{-1}), and GASC20 (1744 m^2 g^{-1}). Besides, the specific capacitance retention of GASC10 (198 F g^{-1}) reached up

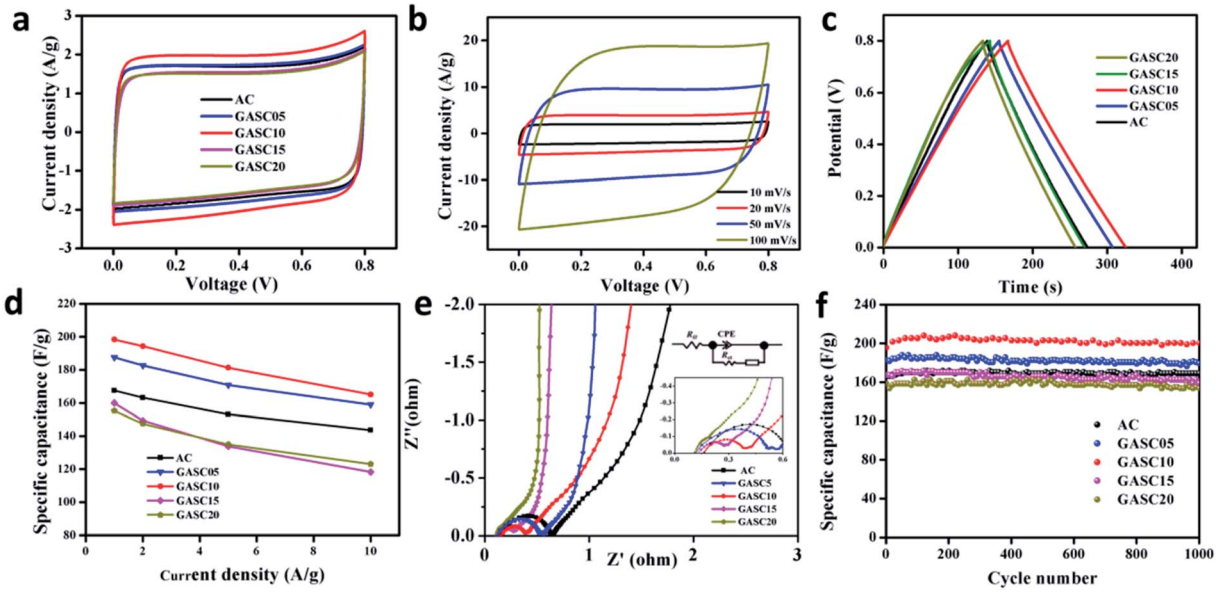

Fig. 5 Electrochemical performance of SCs based on AC, GASC05, GASC10, GASC15, and GASC20 samples in 6 M KOH solution. (a) CV curves at a scan rate of 10 mV s^{-1}; (b) CV curves of GASC10 at different scan rates between 10 mV s^{-1} and 100 mV s^{-1}; (c) charge–discharge curves at a current density of 1 A g^{-1}; (d) specific capacitances at various current densities; (e) Nyquist plots; (f) cycling performance at 1 A g^{-1}.

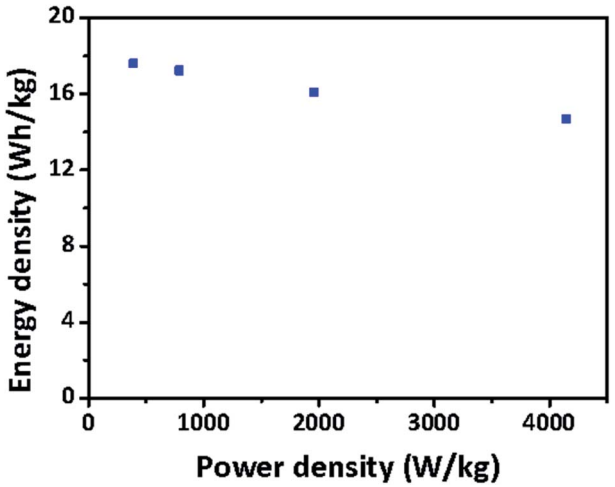

Fig. 6 Ragone plot of GASC10 SSC.

to 83.3% when the current density was increased from 1 A g^{-1} to 10 A g^{-1}, indicative of good electrochemical reversibility.[4] The kinetic behavior of the electrochemical reactions was explored by EIS measurements and the corresponding Nyquist plots are presented in Fig. 5e. The GASC samples exhibit a smaller semicircle than AC implying smaller charge transfer resistance. The charge transfer resistance decreases in the order of AC < GASC05 < GASC10 < GASC15 < GASC20, confirming that the catalytic graphitization can effectively improve the electronic conductivity of GASC samples. The resistivity of the sample was also tested on a four-probe powder conductivity tester and the result is provided in Table S1.† GASC10 (0.187 Ω cm) showed a sharp decrease in resistivity compared to AC (1.536 Ω cm), further confirming improved electronic transfer. The long-life stability of the GASC SSCs was also evaluated and compared to that of an AC-based supercapacitor (Fig. 5f). All the assembled SSCs can maintain their initial specific capacitances well after 1000 cycles at a current density of 1 A g^{-1}. Particularly, the GASC10 SSC retains 99.0% of its initial specific capacitance, which was still much higher than that of the AC SSC, exhibiting excellent cycle stability and promising application potential. To more realistically evaluate the energy storage performance of the supercapacitors, the Ragone plot reflecting the relationship between the energy density and power density of the GASC-based supercapacitors is presented in Fig. 6. The as-optimized GASC10 SSC manifests a high energy density of 17.6 W h kg^{-1} at a power density of 390.18 W kg^{-1} at 1 A g^{-1}. Remarkably, a high energy density of 14.67 W h kg^{-1} can be maintained at a high power density of 4142.80 W kg^{-1} at 10 A g^{-1}, suggesting impressive energy storage capability and rate performance compared with previously reported related materials.[13,22,28–32] Therefore, we can conclude that this outstanding energy storage performance of GASC-based supercapacitors is the result of improvement in the carbon electrode material. The highly graphitized carbon microspheres with a large specific surface area and rich pore structure benefit the electron and mass transfer.

4. Conclusions

In summary, this work demonstrated an *in situ* catalytic graphitization–activation strategy for the construction of carbon microsphere electrode materials with a highly graphitized and pore-rich structure for energy storage in supercapacitors. The tuned structure with a large specific surface area and high graphitization degree endowed the as-assembled SSCs with increased energy storage capability. The optimized GASC10 SSC exhibited a high specific capacitance of 198 F g^{-1} at 1 A g^{-1} and retained 83.3% of its initial capacitance when the current density was increased to 10 A g^{-1}, suggesting robust rate performance. Besides, the GASC10 SSC possessed a high energy density of 14.67 W h kg^{-1}, a power density of 4142.80 W kg^{-1} and long-term stability with 99.0% capacitance retention after 1000 cycles, which is the result of enhanced electron/mass transfer benefiting from the high graphitization degree and large specific surface area of the GASC10 electrode material. This work highlights the significance of tuning the graphitization degree and pore structure of carbon electrode materials derived from biomass for boosted energy storage.

Conflicts of interest

The authors declare no conflict of interest.

Acknowledgements

We are grateful for the support provided by the Special Fund for Guangxi Distinguished Expert, Guangxi Innovation Driven Development Subject (GUIKE AA19182020 and GUIKE AA19254004), and Guangxi Technology Base and Talent Subject (GUIKE AD19110134 and GUIKE AD18126001).

References

1 Y. Zhong, T. Shi, Y. Huang, S. Cheng, G. Liao and Z. Tang, *Electrochim. Acta*, 2018, **269**, 676–685.
2 W. Yuan, Y. Feng, A. Xie, X. Zhang, F. Huang, S. Li, X. Zhang and Y. Shen, *Nanoscale*, 2016, **8**, 8704–8711.
3 J. A. Vigil, T. N. Lambert and B. T. Christensen, *J. Mater. Chem. A*, 2016, **4**, 7549–7554.
4 Y. Gao, Y. Xia, H. Wan, X. Xu and S. Jiang, *Electrochim. Acta*, 2019, **301**, 294–303.
5 E. Senthilkumar, V. Sivasankar, B. R. Kohakade, K. Thileepkumar, M. Ramya, G. Sivagaami Sundari, S. Raghu and R. A. Kalaivani, *Appl. Surf. Sci.*, 2018, **460**, 17–24.
6 Z. Pu, I. Saana Amiinu, M. Wang, Y. Yang and S. Mu, *Nanoscale*, 2016, **8**, 8500–8504.
7 M. R. Benzigar, S. N. Talapaneni, S. Joseph, K. Ramadass, G. Singh, J. Scaranto, U. Ravon, K. Al-Bahily and A. Vinu, *Chem. Soc. Rev.*, 2018, **47**, 2680–2721.
8 Y. Zhou, Z. Zhu, C. Zhao, K. Zhang, B. Wang, C. Zhao and G. Chen, *ACS Sustainable Chem. Eng.*, 2019, **7**, 5095–5102.
9 K. S. Kumar, N. Choudhary, Y. Jung and J. Thomas, *ACS Energy Lett.*, 2018, **3**, 482–495.

10 H. Lyu, J. Zhu, B. Zhou, H. Cao, J. Duan, L. Chen, W. Jin and Q. Xu, *Carbon*, 2018, **139**, 740–749.
11 A. Borenstein, O. Hanna, R. Attias, S. Luski, T. Brousse and D. Aurbach, *J. Mater. Chem. A*, 2017, **5**, 12653–12672.
12 W. Hong, L. Wang, K. Liu, X. Han, Y. Zhou, P. Gao, R. Ding and E. Liu, *J. Alloys Compd.*, 2018, **746**, 292–300.
13 Z. Shang, X. An, H. Zhang, M. Shen, F. Baker, Y. Liu, L. Liu, J. Yang, H. Cao, Q. Xu, H. Liu and Y. Ni, *Carbon*, 2020, **161**, 62–70.
14 X. Zhang, Y. Chen, J. Yan, K. Zhu, M. Zhang, K. Ye, G. Wang, L. Zhou, K. Cheng and D. Cao, *Chem. Eng. J.*, 2020, **388**, 124197–124204.
15 J. Wang, Z. He, X. Tan, T. Wang, L. Liu, X. He, X. D. Liu, L. Zhang and K. Du, *Carbon*, 2020, **160**, 71–79.
16 M.-C. Liu, C. Lu, Y. Xu, Y.-X. Hu, J. Li, H. Zhang, Y.-S. Zhang, B.-M. Zhang, L.-B. Kong, W.-W. Liu, W.-J. Niu, K. Zhao, L. Lee, Z. M. Wang and Y.-L. Chueh, *ACS Sustainable Chem. Eng.*, 2019, **7**, 18690–18699.
17 P. Liu, W. Cai, J. Wei, Z. Cai, M. Zhu, B. Han, Z. Yang, J. Chen and M. Jaroniec, *J. Mater. Chem. A*, 2019, **7**, 18840–18845.
18 Z. Miao, Y. Huang, J. Xin, X. Su, Y. Sang, H. Liu and J. J. Wang, *ACS Appl. Mater. Interfaces*, 2019, **11**, 18044–18050.
19 B. A. Ali, A. M. A. Omar, A. S. G. Khalil and N. K. Allam, *ACS Appl. Mater. Interfaces*, 2019, **11**, 33955–33965.
20 J. S. Shaikh, N. S. Shaikh, R. Kharade, S. A. Beknalkar, J. V. Patil, M. P. Suryawanshi, P. Kanjanaboos, C. K. Hong, J. H. Kim and P. S. Patil, *J. Colloid Interface Sci.*, 2018, **527**, 40–48.
21 L. Yu, Y. Xiao, C. Luan, J. Yang, H. Qiao, Y. Wang, X. Zhang, X. Dai, Y. Yang and H. Zhao, *ACS Appl. Mater. Interfaces*, 2019, **11**, 6890–6899.
22 X. Xu, W. Zhong, X. Zhang, J. Dou, Z. Xiong, Y. Sun, T. Wang and Y. Du, *J. Colloid Interface Sci.*, 2019, **543**, 147–155.
23 L.-F. Zhai, S.-Y. Kong, H. Zhang, W. Tian, M. Sun, H. Sun and S. Wang, *Chem. Eng. Sci.*, 2019, **194**, 45–53.
24 M. Yang, D. Wu and D. Cheng, *Int. J. Hydrogen Energy*, 2019, **44**, 6525–6534.
25 X. Li, Y. Tang, J. Song, W. Yang, M. Wang, C. Zhu, W. Zhao, J. Zheng and Y. Lin, *Carbon*, 2018, **129**, 236–244.
26 F. Yue, G. Gao, F. Li, Y. Zheng and S. Hou, *Carbon*, 2018, **134**, 112–122.
27 B. Chang, W. Shi, S. Han, Y. Zhou, Y. Liu, S. Zhang and B. Yang, *Chem. Eng. J.*, 2018, **350**, 585–598.
28 J. Cao, C. Zhu, Y. Aoki and H. Habazaki, *ACS Sustainable Chem. Eng.*, 2018, **6**, 7292–7303.
29 J. Li, X. Li, D. Xiong, L. Wang and D. Li, *Appl. Surf. Sci.*, 2019, **475**, 285–293.
30 Y. Wang, R. Liu, Y. Tian, Z. Sun, Z. Huang, X. Wu and B. Li, *Chem. Eng. J.*, 2019, 123263–123272.
31 M. Wu, P. Ai, M. Tan, B. Jiang, Y. Li, J. Zheng, W. Wu, Z. Li, Q. Zhang and X. He, *Chem. Eng. J.*, 2014, **245**, 166–172.
32 T. Chen, M. Li, S. Song, P. Kim and J. Bae, *Nano Energy*, 2020, **71**, 104549–104556.